

© 2019 by Akshat Puri. All rights reserved.

MEASUREMENT OF ANGULAR AND MOMENTUM DISTRIBUTIONS OF CHARGED
PARTICLES WITHIN AND AROUND JETS IN Pb+Pb AND $p\bar{p}$ COLLISIONS AT
 $\sqrt{S_{NN}} = 5.02$ TeV WITH ATLAS AT THE LHC

BY
AKSHAT PURI

DISSERTATION

Submitted in partial fulfillment of the requirements
for the degree of Doctor of Philosophy in Physics
in the Graduate College of the
University of Illinois at Urbana-Champaign, 2019

Urbana, Illinois

Doctoral Committee:

Professor Matthias Grosse Perdekamp, Chair
Professor Anne Marie Sickles, Advisor
¹ Professor Aida El-Khadra
Professor Bryce Gadaway

Abstract

² Studies of the fragmentation of jets into charged particles in heavy-ion collisions can help in understanding
³ the mechanism of jet quenching by the hot and dense matter created in such collisions, the quark-gluon
⁴ plasma. This thesis presents a measurement of the angular distribution of charged particles around the jet
⁵ axis as measured in Pb+Pb and pp collisions collided at a center of mass energy of $\sqrt{s_{NN}} = 5.02$ TeV. The
⁶ measurement is done using the ATLAS detector at the Large Hadron Collider, and utilizes 0.49 pb^{-1} of
⁷ Pb+Pb and 25 pb^{-1} of pp data collected in 2015. The measurement is performed for jets reconstructed
⁸ with the anti- k_t algorithm with radius parameter $R = 0.4$, and is extended to regions outside the jet cone.
⁹ Results are presented as a function of Pb+Pb collision centrality, and both jet and charged-particle transverse
¹⁰ momenta. It was observed that in Pb+Pb collisions there is a broadening of the jet for charged particles with
¹¹ $p_T < 4$ GeV, along with a narrowing for charged particles with $p_T > 4$ GeV. Ratios between the angular
¹² distributions in Pb+Pb and pp showed an enhancement for particles with $p_T < 4$ GeV in Pb+Pb collisions,
¹³ with the enhancement increasing up to 2 for $r < 0.3$, and remaining constant for $0.3 < r < 0.6$. Charged
¹⁴ particles with $p_T > 4$ GeV show a small enhancement in the jet core for $r < 0.05$, with a growing suppression
¹⁵ of up to 0.5 for $r < 0.3$ in Pb+Pb collisions. The depletion remains constant for $0.3 < r < 0.6$.

For my Mother, Father, and Brother

¹⁸ Contents

¹⁹ Chapter 1	Introduction	1
²⁰ Chapter 2	Theoretical Introduction	3
²¹ 2.1	Quantum Chromodynamics	3
²² 2.2	Heavy Ion Collisions	6
²³ 2.3	Quark Gluon Plasma	11
²⁴ 2.4	Jets and Jet Quenching	13
²⁵ 2.4.1	Jet Reconstruction	17
²⁶ Chapter 3	Major Jet Measurements	21
²⁷ 3.1	Dijet Balance: x_J	21
²⁸ 3.2	Modification of jet yields: R_{AA}	22
²⁹ 3.3	Jet Fragmentation	25
³⁰ Chapter 4	Experimental Setup	26
³¹ Chapter 5	ATLAS Qualification Task	27
³² Chapter 6	Measurement of Angular Correlations Between Tracks And Jets	28

Chapter 1

Introduction

33 The Large Hadron Collider (LHC) at the European Center for Nuclear Research (CERN), is one of the worlds
34 most expensive and complicated machines. It was built with the purpose of accelerating subatomic particles
35 to close to the speed of light and colliding them to study their underlying structure. Detectors around the
36 LHC ring, the biggest of which are ATLAS (A Toroidal LHC ApparatuS), CMS (Compact Muon Solenoid),
37 ALICE (A Large Ion-Collider Experiment), and LHCb (LHC-Beauty), study these collisions and use the
38 debris as a playground to verify and expand the "Standard Model" of particle physics. This thesis will focus
39 on measurements of collisions involving heavy ions as measured by the ATLAS detector.

40 Relativistic heavy ion collisions such as those at the LHC provide insight into the interactions between
41 quarks and gluons. These fundamental building blocks of all matter interact via the strong force, the
42 theoretical framework of which is described by Quantum Chromodynamics (QCD). This theory dictates
43 that quarks and gluons are confined, i.e. locked together to form composite particles and cannot exist
44 independently, making their study extremely difficult. Relativistic heavy ion collisions provide an extreme
45 environment where nuclear matter can "melt" and form a deconfined medium that consists of free quarks
46 and gluons. This state of matter, called the Quark Gluon Plasma (QGP) is what existed a few microseconds
47 after the Big Bang, and is what eventually cooled and expanded to form the existing universe. It

48 The quark-gluon plasma (see Refs. [1, 2] for recent reviews) can be probed by jets, sprays of particles that
49 come from hard scattering processes between the nucleons involved in the collision. These jets are produced
50 early in the collision and interact with the QGP as they make their way to the detector. Studying the rates
51 and characteristics of these jets in Pb+Pb collisions, and comparing them to similar quantities in pp collisions
52 can provide information on the properties of the QGP. In particular, studying the fragmentation pattern of
53 these jets and how the energy is distributed around the jet axis can provide more information on the jet
54 structure and put constraints on the medium response to the jet.

55 This thesis is split into 4 main chapters. Chapter 2 briefly describes the general theoretical background
56 on QCD, heavy ion collisions, QGP, and jets, giving context to the measurements discussed in this thesis.
57 Chapter 3 will briefly discuss major jet measurements done by the ATLAS Heavy Ion Group. Chapter 4

58 gives an overview of the LHC and the ATLAS detector. Chapter 5 will describe the work undertaken to
59 become a member of the ATLAS Collaboration, and Chapter 6 will provide a detailed description of the
60 measurement to determine the angular distributions of charged particles in Pb+Pb and pp collisions.

Chapter 2

Theoretical Introduction

61 This section shall discuss the theoretical background necessary to understand jet measurements. It will
62 discuss the fundamentals of quantum chromodynamics (QCD), the heavy ion collision system and the quark
63 gluon plasma that is formed, and finally jets and jet energy loss.

64 2.1 Quantum Chromodynamics

65 Quantum Chromodynamics is a gauge theory with SU(3) symmetry that describes the dynamics of the strong
66 interactions between quarks and gluons. It is part of the Standard Model [3], the building blocks of which
67 are shown in Figure 2.1.

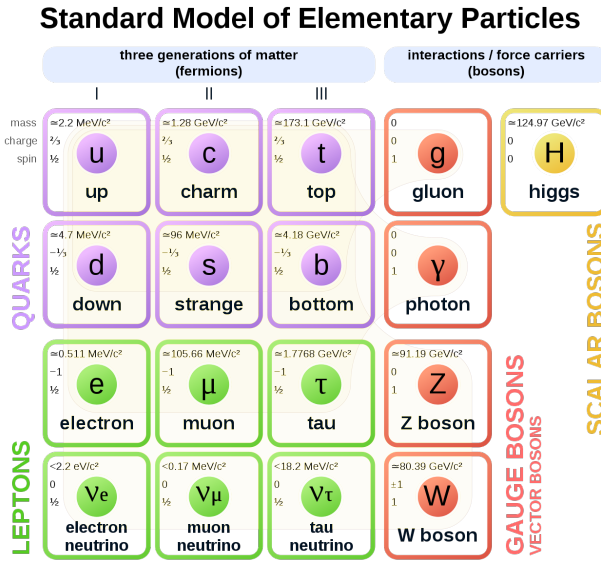


Figure 2.1: The elementary particles of the standard model.

68 Quarks are fermions with a spin of 1/2, and carry a fractional electric charge as well as a color charge.
69 They all have mass and come in six flavors: up, down, top, bottom, strange, charm. The lightest quarks

70 (u and d) combine and form stable particles, while the heavier quarks can only be produced in energetic
 71 environments and decay rapidly. Gluons are gauge bosons (force carriers) with a spin of 1, and are what hold
 72 quarks together. The dynamics of the quarks and gluons are described by the QCD Lagrangian given as [4]:

$$\mathcal{L}_{\text{QCD}} = \sum_q \bar{\psi}_{q,a} (i\gamma^\mu \partial_\mu \delta_{ab} - g_s \gamma^\mu t_{ab}^C \mathcal{A}_\mu^C - m_q \delta_{ab}) \psi_{q,b} - \frac{1}{4} F_{\mu\nu}^A F^{A\mu\nu} \quad (2.1)$$

73 where $\psi_{q,a}$ and $\psi_{q,b}$ are quark-filled spinors for a quarks with flavor q , mass m_q , and color a and b respectively,
 74 with the values for a and b ranging from 1 to 3 (for the three colors). The \mathcal{A}_μ^C corresponds to the gluon field
 75 with C taking values from 1 through 8 (for the 8 types of gluons). The t_{ab}^C corresponds to the Gell-Mann
 76 matrices that are the generators of the SU(3) group, and dictate the rotation of the quarks color in SU(3)
 77 space when it interacts with a gluon. The coupling constant is encoded within g_s , which is defined by
 78 $g_s \equiv \sqrt{4\pi\alpha_s}$. The field tensor $F_{\mu\nu}^A$ can be written in terms of the structure constants of the SU(3) group
 79 f_{ABC} , and is given by:

$$F_{\mu\nu}^A = \partial_\mu \mathcal{A}_\nu^A - \partial_\nu \mathcal{A}_\mu^A - g_s f_{ABC} \mathcal{A}^B \mathcal{A}^C \quad (2.2)$$

80 While many parallels can be drawn between Quantum Electrodynamics (QED, the theory that describes
 81 photons and electrons) and QCD, the difference between the two comes from the gluon-gluon interactions
 82 allowed in QCD, making it non-Abelian. These interactions can be summarized as shown in Figure 2.2.

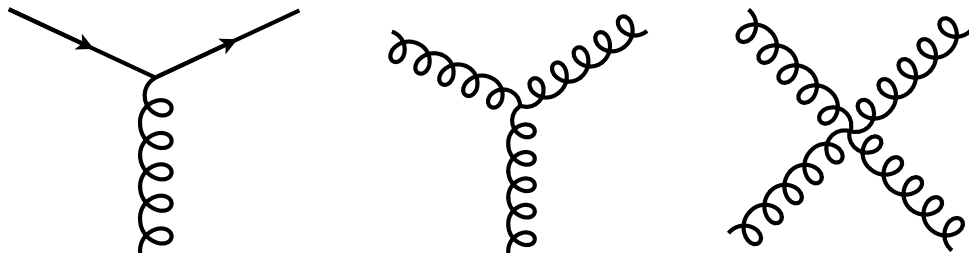


Figure 2.2: The allowed vertices in QCD. The vertices involving two or more gluons are unique to QCD and do not have a QED analog.

83 A core feature of QCD is that the coupling constant α_s has an energy dependence shown in Figure 2.3.
 84 This dependence can be expressed in terms of the β function as

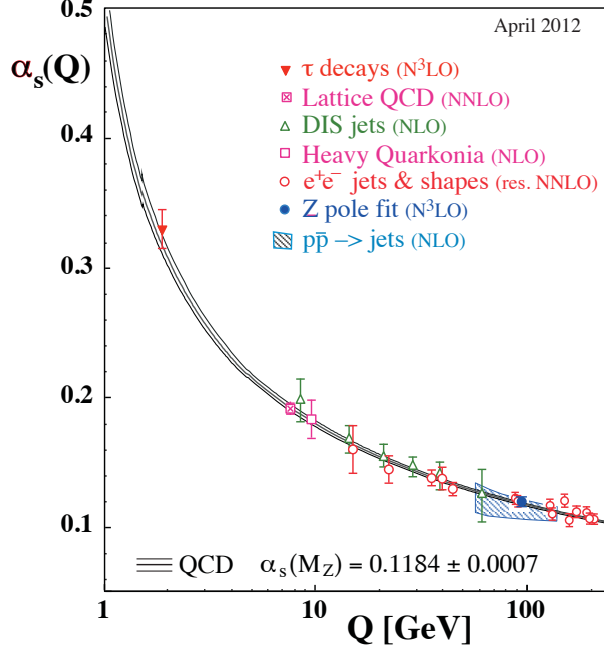


Figure 2.3: The running coupling constant α_s as a function of the momentum transfer Q . Figure taken from Ref. [4].

$$Q^2 \frac{\partial \alpha_s(Q^2)}{\partial Q^2} = \beta(\alpha_s(Q^2)) \quad (2.3)$$

where Q is the momentum transfer in the particle reaction. The beta function can be expressed using perturbative QCD (pQCD) as

$$\beta(\alpha_s) = -(b_0 \alpha_s^2 + b_1 \alpha_s^3 + b_2 \alpha_s^4 \dots) \quad (2.4)$$

where the coefficients b_i depend on the number of colors and flavors.

This running coupling constant is small and asymptotically tends to zero at large energy scales (or at small distances) and is large at small energy scales (large distances). This running coupling phenomenon leads to two key behaviors: asymptotic freedom and color confinement.

Asymptotic Freedom: At high energy scales (small distances), the QCD coupling constant α_s is small and tends to zero, implying a free particle behavior of quarks and gluons. This has been observed by a

93 variety of deep inelastic experiments [5–18]

94 **Color Confinement** The opposite end of the running coupling constant phenomenon is color confinement. This property of QCD forbids the direct observation of free quarks and gluons, allowing only for
95 composite particles that are color singlets.
96

97

98 2.2 Heavy Ion Collisions

99 Heavy ion collisions can be used as a tool to study the Quark Gluon Plasma [19] . They provide access to
100 the otherwise confined partons, and give insight into the QCD phase diagram and the transition between the
101 QGP and hadronic matter.

102 In a heavy ion collision, the colliding nuclei are accelerated to relativistic energies and are Lorentz
103 contracted discs. In the case of a Pb+Pb collision the relativistic γ factor is between 100 and 2500 for
104 beam rapidities of $y = 5.3$ and 8.5 . Each nucleus contains many colored quarks and antiquarks, with three
105 more quarks than anti-quarks per nucleon, with the $q\bar{q}$ popping in and out of the vacuum due to quantum
106 fluctuations. These $q\bar{q}$ pairs are sources of transverse color fields and the corresponding force carriers, the
107 gluons.

108 When these pancake like discs collide, their color fields interact and there is a color charge exchange,
109 producing longitudinal color fields that fill the space between the receding discs. While the maximum energy
110 density in the process occurs just at the collision, the energy density 1 fm/c after the collision is 12 GeV/fm^3 ,
111 much higher than the 500 MeV/fm^3 in a typical hadron. Lattice QCD calculations in thermodynamics show
112 that at these energies, the partons produced in the collision cannot be treated as a collection of distinct
113 hadrons.

114 After the collision the energy density between the receding nuclei starts to decrease as the QGP cools and
115 expands. This process, seen in Figure 2.4, continues till the energy density drops to below that within a
116 hadron and the fluid “hadronizes”. These individual hadrons briefly scatter off of each other before they
117 freely fly towards the detector (freeze-out).

118 While Figure 2.4 shows snapshots of a head on (central) collision between two large nuclei, it is possible to
119 have collisions where the impact parameter is larger and hence the overlap region is smaller. These collisions,
120 called peripheral collisions, qualitatively undergo the same process described above, with the size and shape
121 of the QGP being different.

122 The basic parameters of a heavy ion collision such as the number of participants N_{part} and number of

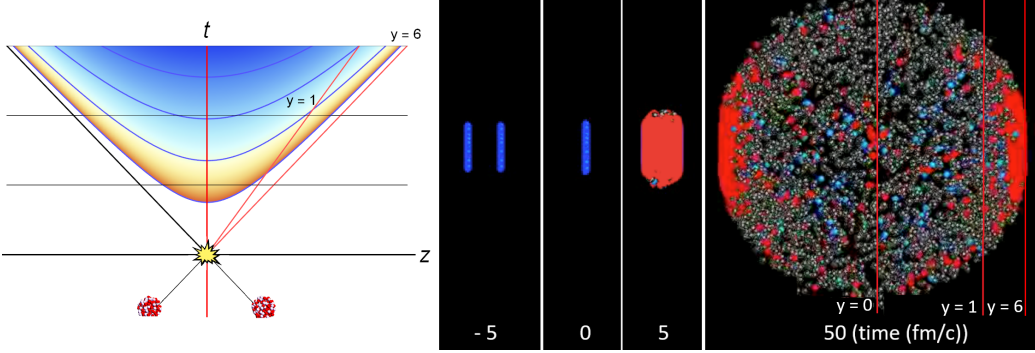


Figure 2.4: (left) Space-time diagram for a heavy ion collision. The color is indicative of the temperature of the QGP formed. (right) Snapshots of a heavy ion collision at $\sqrt{s_{NN}} = 2.76$ TeV at different times. The Lorentz contracted nuclei are in blue while the QGP is in red. Figure from Reference [2].

binary collisions N_{coll} can be determined using the Glauber Monte Carlo simulations [20, 21]. This technique considers a nucleus-nucleus collision as a collection of independent binary nucleon-nucleon collisions; the colliding nuclei are modeled as a set of uncorrelated nucleons being positioned within the nucleus based on a the nuclear density function uniform in azimuthal and in polar angles. The nuclear density function shown in Figure 2.5 for Au and Cu, is given by:

$$\rho(r) = \rho_0 \frac{1 + w(r/R)^2}{1 + e^{\frac{r-R}{a}}} \quad (2.5)$$

where ρ_0 is the nucleon density, R is the nuclear radius, a is the skin depth, w corresponds to deviations from a circular shape and is typically zero for larger nuclei like Cu, W, Au, Pb, and U. For the Pb nuclei used at the LHC, $w = 0$, $R = 6.62$ fm and $a = 0.55$ fm [22].

They are then arranged with a random impact parameter b based on the distribution $d\sigma/db = 2\pi b$ and projected onto the $x - y$ plane as shown in Figure 2.6. They are then made to travel on straight trajectories, colliding if $d \leq \sqrt{\sigma_{\text{inel}}^{\text{NN}}/\pi}$, where d is the distance between the nucleons in a plane transverse to the beam axis and $\sigma_{\text{inel}}^{\text{NN}}$ is the inelastic scattering cross section. [23, 24]

An important parameter for colliding nuclei A and B with A and B nucleons is the thickness function T_{AB} . It describes the effective overlap area in which specific nucleons in the two colliding nuclei can interact. It can be defined in terms of the probability per unit area of a given nucleon being located at a particular distance s within the nucleus. For the colliding nuclei A and B, this is given by $T_A(\mathbf{s}) = \int \rho_A(\mathbf{s}, z_A) dz_A$ and $T_B(\mathbf{s}) = \int \rho_B(\mathbf{s}, z_B) dz_B$. Then, T_{AB} is given by

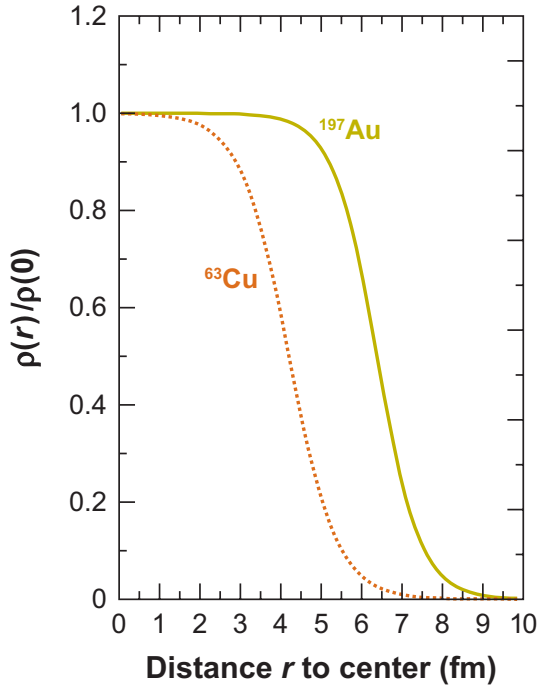


Figure 2.5: The nuclear density distributions for nuclei used at RHIC: Cu ($w = 0$, $R = 4.2$ fm and $a = 0.48$ fm) and Au ($w = 0$, $R = 6.38$ fm and $a = 0.535$ fm) [22, 23].

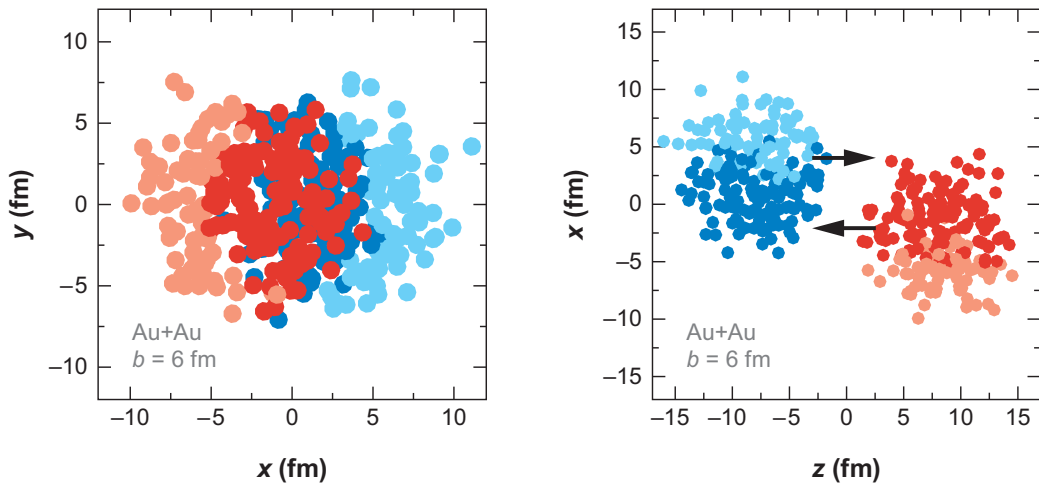


Figure 2.6: A Glauber Monte Carlo event for $\text{Au} + \text{Au}$ at $\sqrt{s_{\text{NN}}} = 200$ GeV with impact parameter of 6 fm viewed in the (left) transverse plane and (right) along the beam axis. Darker circles represent the participating nucleons. Taken from [23].

$$T_{AB}(\mathbf{b}) = \int T_A(\mathbf{s})T_B(\mathbf{s} - \mathbf{b})d^2s \quad (2.6)$$

140 The probability of then having n interactions between nuclei A and B is given by the binomial distribution:

$$P(n, \mathbf{b}) = \binom{AB}{n} \left[T_{AB}(\mathbf{b})\sigma_{\text{inel}}^{\text{NN}} \right]^n \left[1 - T_{AB}(\mathbf{b})\sigma_{\text{inel}}^{\text{NN}} \right]^{AB-n} \quad (2.7)$$

141 where the first term is the number of combinations for finding n collisions from AB possibilities, the
142 second term is the probability for having exactly n collisions, and the last term the probability of $AB - n$
143 misses. Then the total probability of an interaction between A and B is

$$\frac{d^2\sigma_{\text{inel}}^{\text{AB}}}{db^2} \equiv p_{\text{inel}}^{\text{AB}}(b) = \sum_{n=1}^{AB} P(n, \mathbf{b}) = 1 - \left[1 - T_{AB}(\mathbf{b})\sigma_{\text{inel}}^{\text{NN}} \right]^{AB} \quad (2.8)$$

144 Then the total cross section is given by

$$\sigma_{\text{inel}}^{\text{AB}} = \int_0^\infty 2\pi b db \left[1 - \left(1 - T_{AB}(\mathbf{b})\sigma_{\text{inel}}^{\text{NN}} \right)^{AB} \right] \quad (2.9)$$

145 and N_{coll} and N_{part} are given by [25, 26]

$$N_{\text{coll}}(b) = \sum_{n=1}^{AB} n P(n, b) = AB \times T_{AB}(b)\sigma_{\text{inel}}^{\text{NN}} \quad (2.10)$$

$$N_{\text{part}}(b) = A \int T_A(\mathbf{s}) \left[1 - \left(1 - T_B(\mathbf{s} - \mathbf{b})\sigma_{\text{inel}}^{\text{NN}} \right)^B \right] d^2s + B \int T_B(\mathbf{s} - \mathbf{b}) \left[1 - \left(1 - T_A(\mathbf{s})\sigma_{\text{inel}}^{\text{NN}} \right)^A \right] d^2s \quad (2.11)$$

146 The correlation between N_{coll} and N_{part} can be seen in Figure 2.7

147 The charged particle multiplicity N_{ch} along with the combination of N_{part} and impact parameter b can
148 be used to determine the centrality of a heavy ion event. An example of this is shown in Figure 2.8.

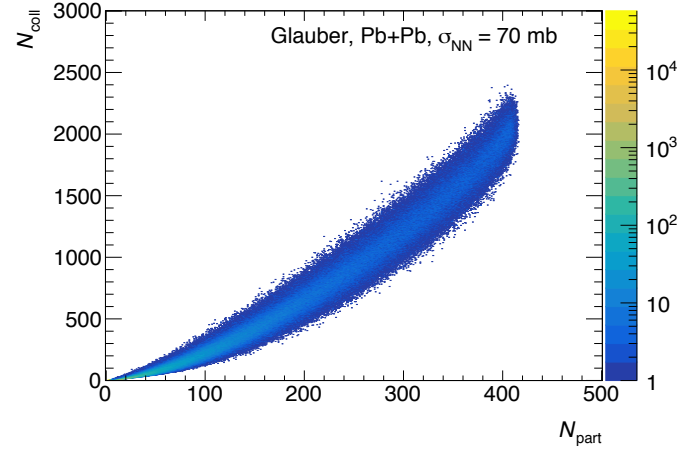


Figure 2.7: The $N_{\text{coll}} - N_{\text{part}}$ correlation for Pb+Pb collisions at $\sqrt{s_{\text{NN}}} = 5.02 \text{ TeV}$. Taken from [27].

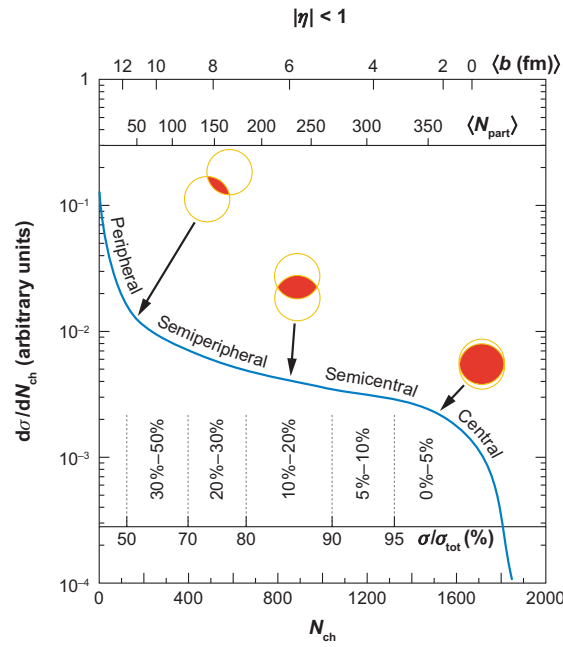


Figure 2.8: The correlation between the observable N_{ch} and N_{part} to determine the centrality distribution. Taken from [23].

2.3 Quark Gluon Plasma

Extreme conditions of temperature and pressure like those in relativistic heavy ion collisions lead to the formation of the Quark Gluon Plasma [19]. It is believed to have filled the early universe a few microseconds after the Big Bang and might be present in the cores of extremely compact objects like neutron stars [28, 29]. The phase transition between the free quarks and gluons within the QGP and the confined quarks and gluons within hadrons can be seen in Figure 2.9.

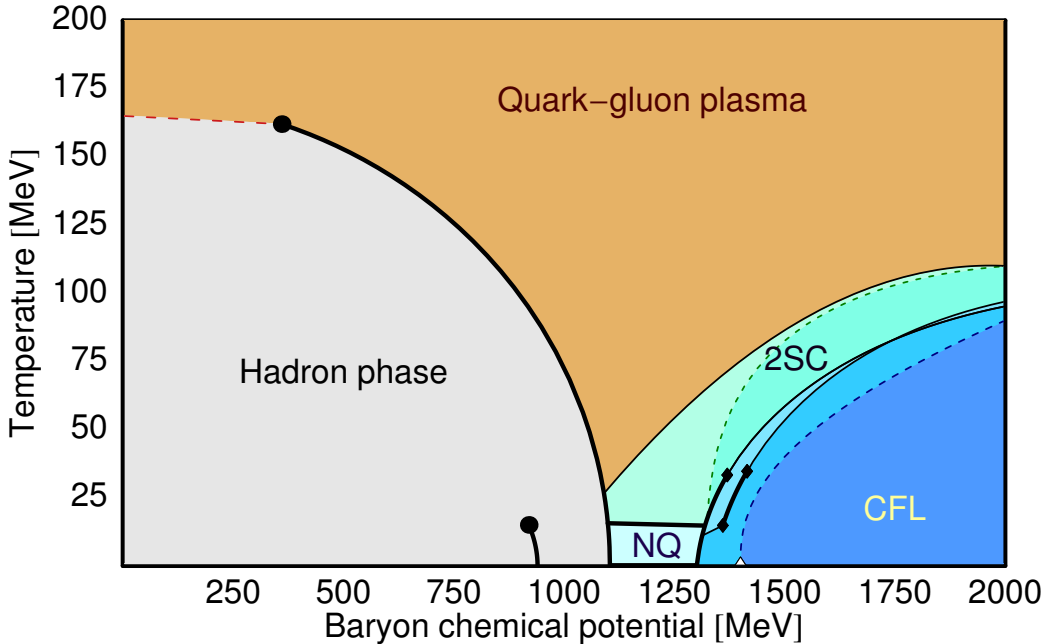


Figure 2.9: The QCD phase diagram of nuclear matter. Figure from Reference [30].

This state of matter exists for 1–10 fm/c, depending on the collision energy, above $\lambda_{\text{QCD}} = 200$ MeV, the fundamental energy scale in QCD. Thermal photons from the QGP reveal that it reaches temperatures of 300–600 MeV in central collisions at 200 GeV [31] and 2.76 TeV [32], showing very little collision energy dependence. Further, the chemical freeze-out temperature was found to be 160 MeV via measurements of ratios of final state hadrons containing the light u, d quarks [33–35] with the thermal freeze-out being 100–150 MeV [36–39]. These measurements paint a picture of the QGP being formed early in the heavy ion collision. It has a non-uniform energy density and temperature determined by the 'colliding nuclei and collision energy'. The QGP then cools and expands as described by relativistic hydrodynamics, and as its temperature falls below 160 MeV, it experiences a crossover phase transition and hadronizes. This system continues to cool and expand, until at 95 GeV there is a thermal freeze-out.

The QGP was initially thought to be a weakly coupled parton gas because of asymptotic freedom from

166 QCD. The highly energetic collisions such as those at the LHC would imply a weak interaction between the
 167 quarks and gluons that make up the plasma. This would result in rare scatterings between the constituents
 168 of the gas and wash out any spatial anisotropies based on the collision geometry. On the other hand, a
 169 strong coupling within the QGP would result in the pressure gradients in the medium being driven by
 170 hydrodynamics and spatial anisotropies would be transformed to momentum anisotropies in the particles
 171 produced as shown in Figure 2.10. In this picture, the non-uniform structure of the colliding nuclei would
 172 cause a momentum anisotropy that would be further enhanced when looking at collisions that are less central
 173 and do not have perfect overlap between the colliding nuclei. These observations were seen in azimuthal
 174 correlation measurements implying that the medium is indeed strongly coupled [40–43].

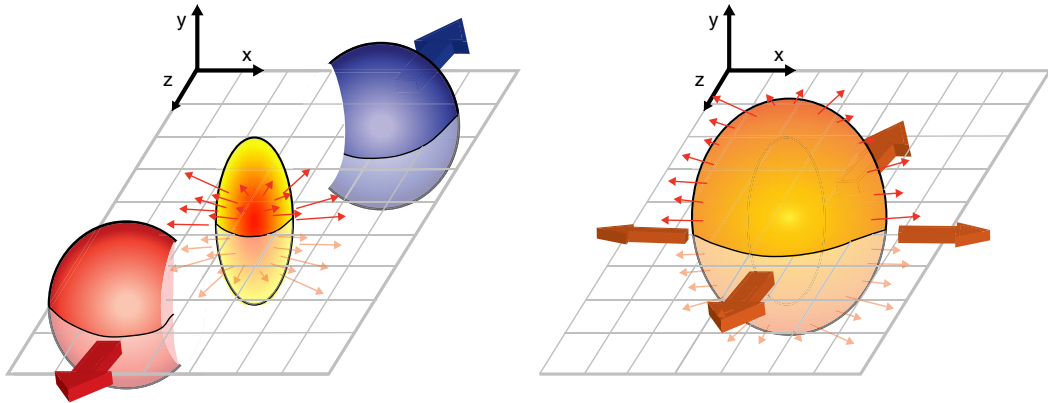


Figure 2.10: Schematic diagrams of the initial overlap region (left) and the final spatial anisotropy generated (right). Taken from [44].

175 A Fourier Transform of the angular distribution of charged hadrons in the collision debris can quantify
 176 these momentum anisotropies and give the anisotropic flow coefficients v_n , defined as [45]:

$$\frac{d\bar{N}}{d\phi} = \frac{\bar{N}}{2\pi} \left(1 + 2 \sum_{n=1}^{\infty} v_n \cos(n(\phi - \bar{\Psi}_n)) \right) \quad (2.12)$$

177 where ϕ is the angle in the transverse plane, $\bar{\Psi}_n$ are the event plane angles, and \bar{N} is the average number
 178 of particles per event. Some of these coefficients are shown in Figure 2.11. The measured anisotropies can be
 179 used to constrain the specific viscosity given by the ratio of viscosity to entropy density, η/s , and have shown
 180 that the QGP has a η/s of near the theoretical minimum of $1/4\pi$ [46].

181 The Bjorken energy density of the QGP can be derived using [49]:

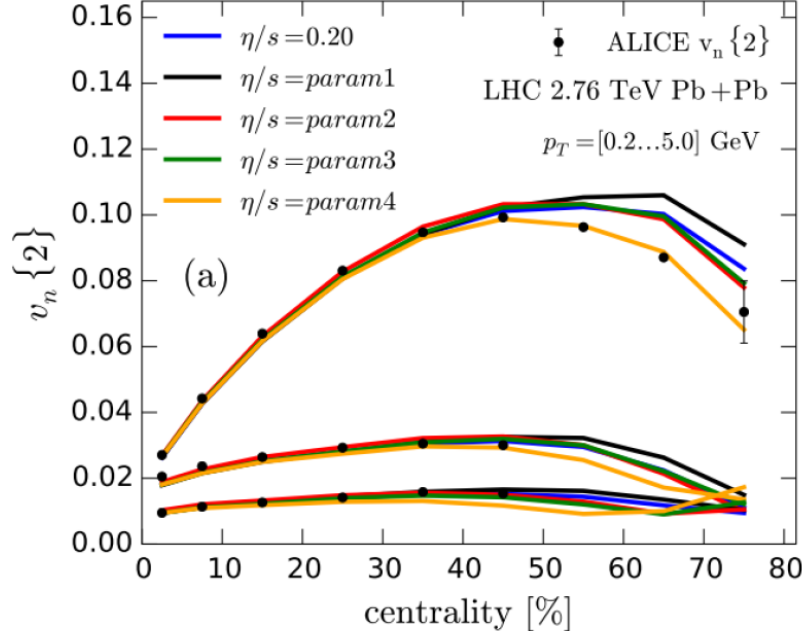


Figure 2.11: Comparison of a hydrodynamic model from [47] to anisotropy measurements by ALICE [48] for different parameterizations of η/s and for different v_n , $n = 2, 3, 4$ from top to bottom, as a function of collision centrality.

$$\varepsilon \geq \frac{dE_{\text{T}}/d\eta}{\tau_0 \pi R^2} = \frac{3}{2} \langle E_{\text{T}}/N \rangle \frac{dN_{\text{ch}}/d\eta}{\tau_0 \pi R^2} \quad (2.13)$$

where $dN_{\text{ch}}/d\eta$ is the number of charged particles produced per unity pseudorapidity, $dE_{\text{T}}/d\eta$ is the transverse energy per unit pseudorapidity, τ_0 is the thermalization time, R is the nuclear radius, and $E_{\text{T}}/N \approx 1$ GeV is the transverse energy per emitted particle. As shown in Figure 2.12, the energy density at the LHC was measured to be approximately 15 GeV/fm^3 , much higher than the values measured at RHIC [50, 51].

2.4 Jets and Jet Quenching

Hard scatterings in particle collisions result in the production of highly energetic partons that form conical sprays of hadrons called jets. A schematic of this process is shown in Figure 2.13. Jet production in a vacuum is well described in context of perturbative QCD [53] where processes involving large momentum transfers like high p_{T} hadron production can be described in terms of the parton distribution functions, scattering cross sections, and final state fragmentation functions as shown below [54]:

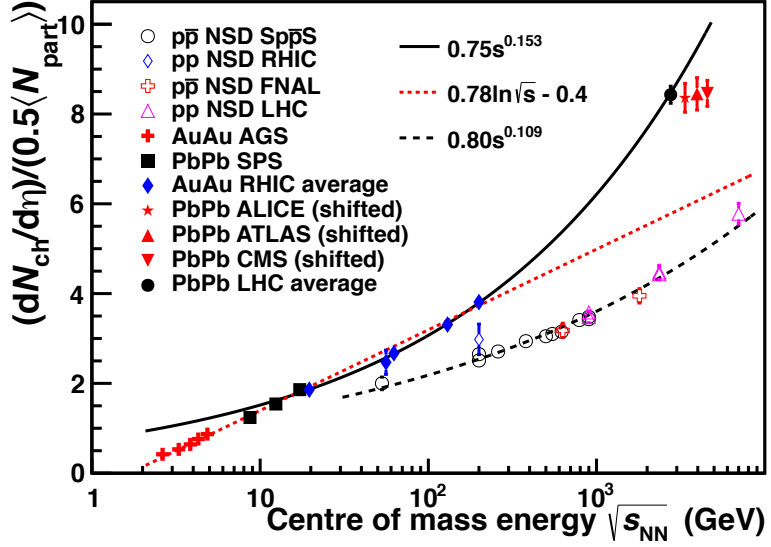


Figure 2.12: $dN_{\text{ch}}/d\eta$ per colliding nucleon pair as a function of collision energy in pp and nucleus-nucleus collisions [52].

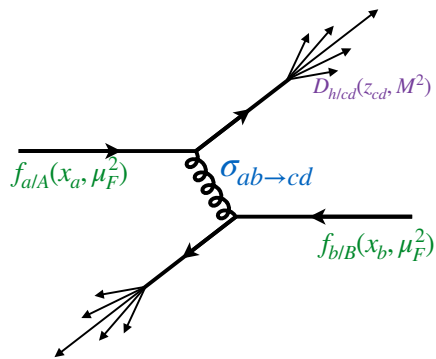


Figure 2.13: Jet production from the process $pp \rightarrow hX$, factorizing in terms of the parton distribution functions, scattering cross sections, and jet fragmentation functions. [54]

$$\begin{aligned}
d\sigma_{pp \rightarrow hX} &\approx \sum_{abjd} \int dx_a \int dx_b \int dz_j f_{a/p}(x_a, \mu_f) \otimes f_{b/p}(x_b, \mu_f) \\
&\otimes d\sigma_{ab \rightarrow jd}(\mu_f, \mu_F, \mu_R) \\
&\otimes D_{j \rightarrow h}(z_j, \mu_f)
\end{aligned} \tag{2.14}$$

where $x_a = p_a/P_A, x_b = p_b/P_b$ are the initial momentum fractions carried by the interacting partons, $z_j = p_h/p_j$ is the momentum fraction carried by the final observed hadron. $f_{a/p}(x_a, \mu_f)$ and $f_{b/p}(x_b, \mu_f)$ are the two parton distribution functions (PDFs), $d\sigma_{ab \rightarrow jd}(\mu_f, \mu_F, \mu_R)$ is the differential cross section for parton scattering and $D_{j \rightarrow h}(z_j, \mu_f)$ is the fragmentation function (FFs) for parton j to hadron h . μ_f and μ_F are the factorization scales and μ_R is the renormalization scale, and are typically taken to be the same hard scale Q . The PDFs characterize the initial state and represent the probability of finding a parton with momentum fraction x (shown in Figure 2.14) in the initial hadron, while the FFs describe the probability of fragmenting to a hadron h with given kinematic properties.

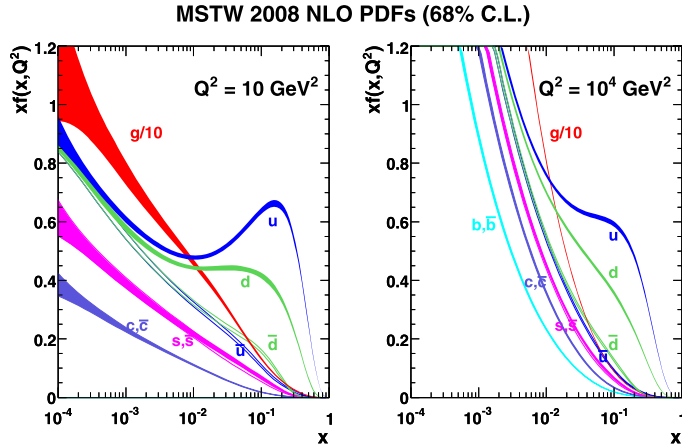


Figure 2.14: The next to leading order (NLO) PDFs at (left) $Q^2 = 10 \text{ GeV}^2$ and (right) $Q^2 = 10^4 \text{ GeV}^2$. The band is the associated one-sigma (68%) confidence level uncertainty. Taken from [55]

In the case of heavy ion collisions, the jet observables can be modified due to two sources: the nuclear PDF being distinct from a proton PDF, and the formation of the quark gluon plasma. The former is collectively referred to as cold nuclear matter (CNM) effect, and can be quantified by defining a nuclear modification factor for the PDF:

$$R_a^A(x, Q^2) = \frac{f_{a/A}(x, Q^2)}{f_{a/p}(x, Q^2)} \quad (2.15)$$

where $f_{a/A}$ and $f_{a/p}$ are the nuclear and proton PDFs respectively. This R_a^A factor is determined by global fits to data from DIS measurements [56–58]. CNM effects include the following contributions:

- Shadowing: This is a destructive interference effect that reduces the interactions of a nucleon incident on a nucleus within its interior and on its back face. This effect reduces the effective number of nucleons in an inelastic interaction to $A^{2/3}$. For Q^2 of the order of a few GeV^2 , this effect dominates for $x < 0.05$ and implies $R_a^A(x, Q^2) < 1$ [59].
- Anti-shadowing: This compensates for the shadowing effect based on the momentum sum rule, and for Q^2 of the order of a few GeV^2 implies $R_a^A(x, Q^2) > 1$ over the region $0.05 < x < 0.20$.
- EMC: The modification of the nuclear structure function was first observed by the European Muon Collaboration [60]. Recent observations have suggested that the effect is caused by short-range correlated nucleon pairs within nuclei [61]. For Q^2 of the order of a few GeV^2 , this effect dominates for $0.2 < x < 0.80$ and implies $R_a^A(x, Q^2) < 1$.
- Fermi Motion: This effect considers the motion of the nucleons within the nucleus. It results in $R_a^A(x, Q^2) > 1$ over the $x > 0.8$ region for Q^2 of the order of a few GeV^2 [62].

Cold nuclear matter effects are experimentally measured using $p + A$ systems where the size and shape of the plasma, and hence any effects thereof, are a lot smaller.

The second source of modification is the formation of the hot and dense quark gluon plasma. The hot nuclear matter effects further serve as an independent confirmation that the medium formed is strongly interacting. Jets are formed early enough that they traverse the Quark Gluon Plasma and as strongly interacting particles, are both affected by, and affect the QGP. This interaction typically results in the jet losing energy and forward momentum [63, 64], with the lost energy being deposited in the medium [65]. Jets can also pick up momentum transverse to the parton direction [66]. The hot nuclear matter effects can be considered to be a combination of collisional and radiative energy losses summarized in Figure 2.15.

- Collisional energy loss: This is a combination of elastic and inelastic collisions of the hard parton with the constituents of the quark gluon plasma.
- Radiative energy loss: This is the larger source of parton energy loss and jet quenching. These are modified by the presence of the plasma due to scatterings off of the plasma constituents. A variety of

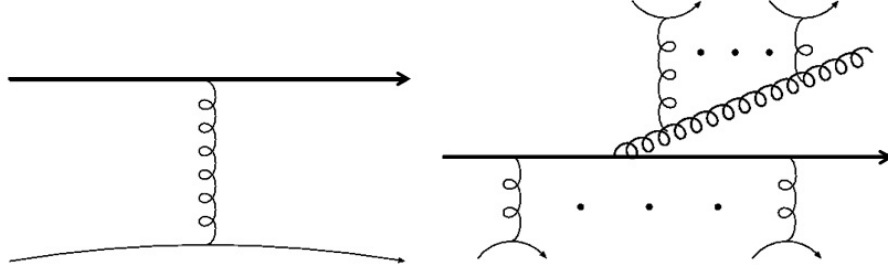


Figure 2.15: The typical diagrams for (left) collisional and (right) radiative energy losses for a parton in a hard scattering as it propagates through the QGP. Taken from [54]

radiative energy loss frameworks that have been developed include: Baier-Dokshitzer-Mueller-Peigne-Schiff-Zakharov (BDMPS-Z) [67], Gyulassy, Levai and Vitev (GLV) [68], Amesto-Salgado-Wiedemann (ASW) [69], Arnold-Moore-Yaffe (AMY) [70] and higher twist (HT) [71].

Both hot and cold nuclear matter effects can be described by modifying Equation 2.14 as:

$$d\sigma_{AB \rightarrow hX} \approx \sum_{abjj'd} f_{a/A}(x_a) \otimes f_{b/B}(x_b) \otimes d\sigma_{ab \rightarrow jd}(\mu_f, \mu_F, \mu_R) \otimes P_{j \rightarrow j'} \otimes D_{h \rightarrow j'}(z_j, \mu_f) \quad (2.16)$$

where the additional $P_{j \rightarrow j'}$ describes the interaction of the hard parton with the colored medium. This is typically taken as part of the fragmentation modification as:

$$\tilde{D}_{h \rightarrow j'}(z_j, \mu_f) \approx \sum_{j'} P_{j \rightarrow j'}(p_{j'}|p_j) \otimes D_{h \rightarrow j'}(j') \quad (2.17)$$

2.4.1 Jet Reconstruction

Jets can be reconstructed by clustering algorithms that take in a variety of inputs. The algorithm used in ATLAS is the anti- k_t clustering algorithm [72]. This algorithm clusters soft particles around hard ones in the following manner:

- Calculate all distances d_{ij} between entities i and j , and distance d_{iB} between entity i and beam B .
- Identify the smallest distances such that for the smallest distance d_{ij} , the entities i and j are combined

242 and return to beginning.

- 243 • If the smallest distance is d_{iB} , then take i as the jet and remove it from the list of entities and return
244 to beginning.
- 245 • Continue the procedure till the list of items is empty.

246 In general the distance d_{ij} between the objects is found the via the prescription

$$d_{ij} = \min(k_{Ti}^{2p}, k_{Tj}^{2p}) \frac{\Delta_{ij}^2}{R^2} \quad (2.18)$$

$$d_{iB} = k_{Ti}^{2p} \quad (2.19)$$

247 where k_{Ti} is the transverse momentum of particle i and $\Delta_{ij} = \sqrt{\Delta\eta_{ij}^2 + \Delta\phi_{ij}^2}$ is the distance between
248 particles i and j in $\eta - \phi$ space. R the distance parameter and reflects the size of the jet being considered. In the
249 case of the anti- k_t algorithm, $p = -1$. Other popular clustering algorithms like k_t [73] and Cambridge/Aachen
250 [74] use $p = 1$ and $p = 0$ respectively. The behavior of the different clustering algorithms is shown in
251 Figure 2.16.

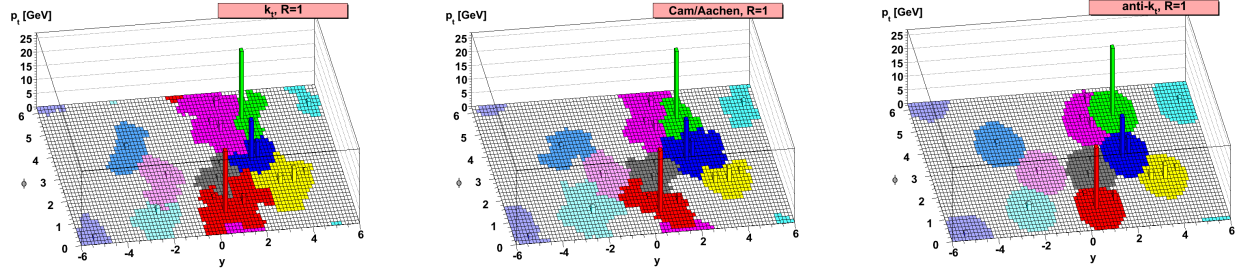


Figure 2.16: Different clustering algorithms applied to the sample parton-level event. Figure taken from [72].

252 The popularity of the anti- k_t algorithm comes from its overcoming of two common problems: collinear
253 and infrared safety. These are related to instabilities in the cones that are found due to soft radiation.

254 Figure 2.17 describes the collinear safety problem. In a collinear safe jet algorithm, the presence of a virtual
255 loop or a collinear splitting of a central particle would not change the number of jets being reconstructed.
256 On the other hand, while a collinear unsafe jet algorithm would not change its output with the presence
257 of a virtual loop, a splitting in the central particle would lead to the left and right most particles forming
258 individual seeds, implying two reconstructed jets [75].

259 A schematic describing infrared safety problem is shown in Figure 2.18. Here an infrared safe algorithm
260 would use the three particles as seeds iteratively find two stable cones. An unsafe algorithm however would

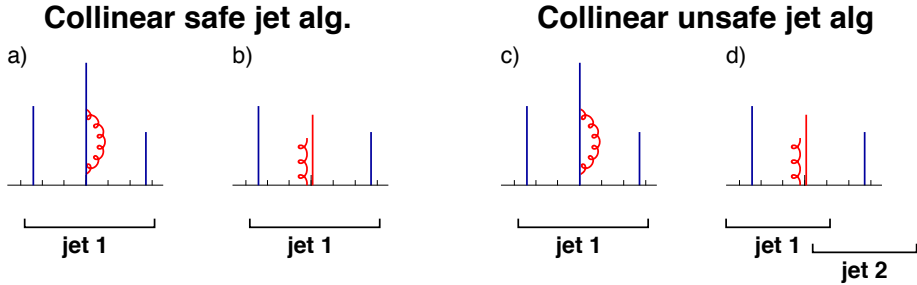


Figure 2.17: An illustration of collinear unsafe behavior. The particle p_T is proportional to the height and the horizontal axis indicates rapidity. Taken from [75].

261 find three overlapping cones based on the addition of a soft seed.

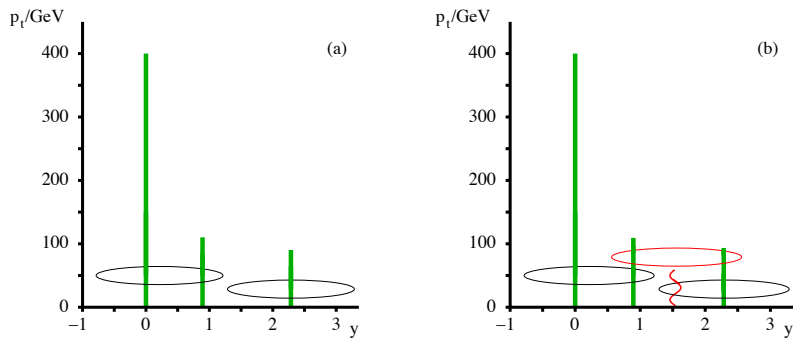


Figure 2.18: An illustration of infrared unsafe behavior. The particle p_T is proportional to the height and the horizontal axis indicates rapidity. Taken from [76].

262 For heavy ion collisions in ATLAS, the inputs to the algorithm are the $\eta \times \phi = 0.1 \times 0.1$ calorimeter
 263 towers. The tower energies are determined by summing up the energies of the individual calorimeter cells.
 264 The anti- k_t algorithm is first run with the distance parameter $R = 0.2$, following which an underlying event
 265 subtraction procedure is performed. A first estimate of the average underlying event energy density $\rho_i(\eta)$ is
 266 done in 0.1 slices of η in each calorimeter layer i after excluding the regions that overlap with the seed jets.
 267 A modulation of $2v_2 \cos[2(\phi - \Psi_2)]$ is applied to account for the flow from the QGP and the underlying event
 268 is subtracted to give E_{Tj}^{sub} :

$$E_{Tj}^{\text{sub}} = E_{Tj} - A_j \rho_i(\eta_j) \left(1 + 2 \sum_{n=2}^4 v_{ni} (\cos[2(\phi - \Psi_n)]) \right) \quad (2.20)$$

269 where E_{Tj}, η_j, ϕ_j and A_j are the cell E_T, η, ϕ and area for cell j in layer i . This process is done iteratively
 270 done one more time after getting new seeds with the distance parameter $R = 0.2$ and excluding areas that
 271 are within $\Delta R = 0.4$ of the seeds. Updated values of ρ'_i and v'_2 are recalculated and used to estimate the

272 background that is subtracted from the original cell energies. More details on this procedure can be found in
273 [77].

Chapter 3

Major Jet Measurements

274 This chapter shall discuss some important experimental jet measurements that motivate the study of the
275 main analysis in this thesis. These include the study of the jet yields, dijet asymmetry, and jet fragmentation.

276 3.1 Dijet Balance: x_J

277 This section will discuss the dijet balance for $R = 0.4$ jets as measured by ATLAS detector for Pb+Pb
278 collisions at $\sqrt{s_{\text{NN}}} = 2.76$ TeV [78]. The dijet imbalance can be expressed in terms of x_J defined as

$$x_J = \frac{p_{\text{T}2}}{p_{\text{T}1}} \quad (3.1)$$

279 where $p_{\text{T}2}$ and $p_{\text{T}1}$ are the transverse momenta of the two highest- p_{T} jets in the event respectively. The
280 minimum $p_{\text{T}2}$ considered is 25 GeV and the pair of jets are separated by $|\Delta\phi| > 7\pi/8$. The dijet yields
281 normalized by the number of jets and determined as $1/N_{\text{jets}} dN/dx_J$ are presented as a function of x_J for
282 different centrality intervals, as well as different ranges for $p_{\text{T}1}$. The measured distributions are further
283 unfolded to remove detector resolution effects and allow comparison to theoretical models.

284 Figure 3.1 shows the x_J distribution for dijet pairs in pp and Pb+Pb collisions in two different centrality
285 bins and two $p_{\text{T}1}$ ranges. It can be seen that the dijet yields in pp are peaked at unity and become narrower
286 for larger $p_{\text{T}1}$ ranges. This reflects the fact that the effects of jet quenching are minimal and the higher- p_{T}
287 jets are better balanced. The dijet yields in peripheral Pb+Pb collisions are similar to the distributions from
288 the pp data, showing that the effects of quenching are smaller. On the other hand, dijet yields in central
289 Pb+Pb collisions are significantly broadened, reflecting the maximal of jet quenching. This is consistent with
290 the picture of the individual jets in the dijet pair traversing different lengths in the QGP and hence losing
291 different amounts of energy. In fact, the distribution for Pb+Pb data is peaked at $x_J = 0.5$, implying a loss
292 of 50% of the jet p_{T} .

293 Further measurements of $R = 0.3$ jets are shown in Figure 3.2. These distributions are significantly flatter

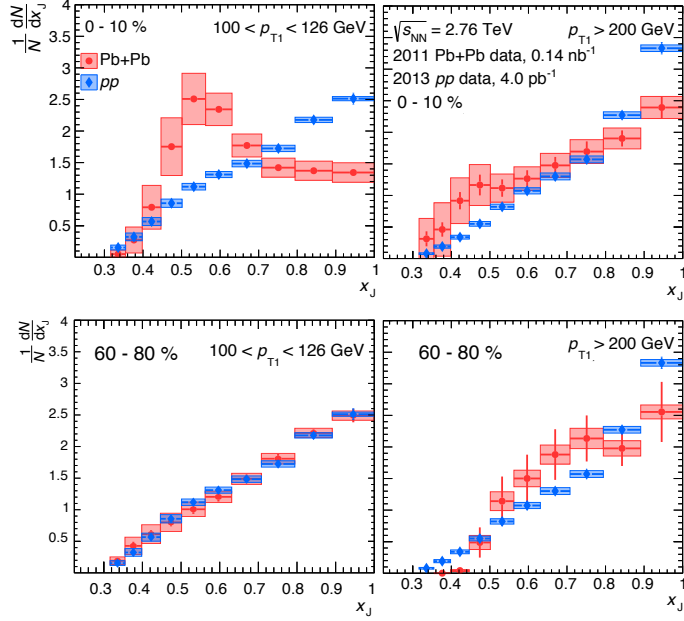


Figure 3.1: The $1/N_{\text{jets}} dN/dx_J$ distributions for $R = 0.4$ jets as a function of x_J for pp (blue) and $\text{Pb}+\text{Pb}$ (red) collisions. The different panels are for (top) central and (bottom) peripheral collisions in (left) $100 < p_{T1} < 126 \text{ GeV}$ and (right) $p_{T1} > 200 \text{ GeV}$. The pp data is the same in all panels. The statistical uncertainties are indicated by the bars while the boxes indicate the systematic uncertainties. Figures taken from [78]

294 than the ones for $R = 0.4$ jets, an observation that is consistent with the expectation that the transverse
 295 momenta correlation between the dijet pair is weaker for jets with smaller radii due to radiation that is
 296 outside the nominal jet cone.

297 3.2 Modification of jet yields: R_{AA}

298 This section discusses the measurement of the inclusive jet R_{AA} as measured by the ATLAS detector for
 299 $R = 0.4$ jets in $\sqrt{s_{\text{NN}}} = 5.02 \text{ TeV}$ $\text{Pb}+\text{Pb}$ collisions [79].

300 While a measurement that compares the jets in a dijet system to each other as discussed in Section 3.1
 301 can provide valuable information about how jets lose energy, it has the following limitation: If both jets lose
 302 equal amounts of energy, the dijet yield will still be peaked at unity and no new information will be obtained.
 303 Thus, it is useful to compare the jet yields directly between the pp and $\text{Pb}+\text{Pb}$ systems and construct the jet
 304 R_{AA} observable. This is defined as:

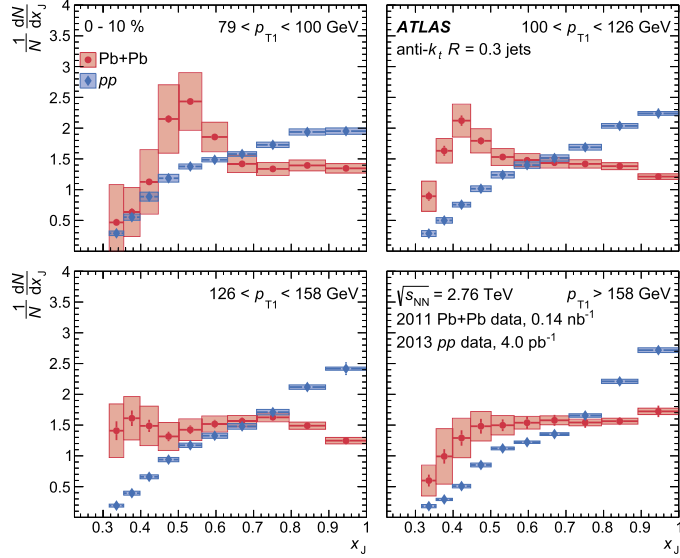


Figure 3.2: The $1/N_{\text{jets}} dN/dx_J$ distributions for $R = 0.3$ jets as a function of x_J in pp and central $\text{Pb}+\text{Pb}$ collisions. The different panels are for different, $p_{\text{T}1}$ ranges (top left to bottom right) central and (bottom) peripheral collisions. The $\text{Pb}+\text{Pb}$ data is in red circles while the pp data is in blue diamonds and is the same in all panels. The statistical uncertainties are indicated by the bars while the boxes indicate the systematic uncertainties. Figures taken from [78]

$$R_{\text{AA}} = \frac{\frac{1}{N_{\text{evt}}} \left. \frac{d^2 N_{\text{jet}}}{dp_{\text{T}} dy} \right|_{\text{cent}}}{\langle T_{\text{AA}} \rangle \left. \frac{d^2 \sigma_{\text{jet}}}{dp_{\text{T}} dy} \right|_{\text{pp}}} \quad (3.2)$$

where T_{AA} is the nuclear thickness function and accounts for the geometric enhancement between pp and $\text{Pb}+\text{Pb}$ as discussed in Section 2.2 and [23].

This measurement was conducted for jets in the 40–1000 GeV range in different rapidity and centrality intervals. The jet yields in pp and $\text{Pb}+\text{Pb}$ collisions are shown in Figure 3.3. The $\text{Pb}+\text{Pb}$ jet yields are scaled by the thickness function and are shown for 8 centrality intervals. Figure 3.4 shows the measured inclusive jet R_{AA} as a function of jet p_{T} for different centrality bins and jet rapidity $|y| < 2.8$. It can be seen that the most central collisions show a clear suppression with an $R_{\text{AA}} \approx 0.45$ at jet $p_{\text{T}} = 100$ GeV. The R_{AA} value slowly evolves with jet p_{T} and rises to 0.6 at jet $p_{\text{T}} = 800$ GeV. This modification becomes smaller for more peripheral collisions. The smooth centrality dependence can be more clearly seen in Figure 3.5, where R_{AA} is shown as a function of $\langle N_{\text{part}} \rangle$ for jets the 100–126 GeV and 200–251 GeV ranges. The magnitude of the suppression is also seen to depend on jet p_{T} for $\langle N_{\text{part}} \rangle \geq 50$.

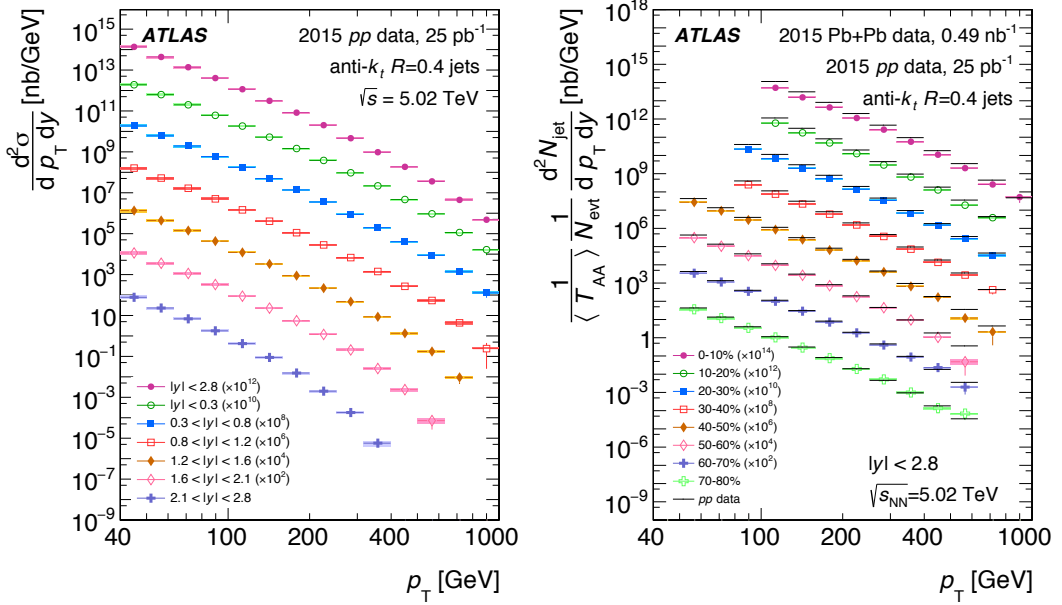


Figure 3.3: (Left) The inclusive jet cross section in pp collisions as a function of jet p_T in different $|y|$ intervals scaled by successive powers of 10^2 for visibility. (Right) Per event inclusive jet yield in $Pb+Pb$ collisions normalized by $\langle T_{AA} \rangle$ as a function of jet p_T in different centrality intervals scaled by successive powers of 10^2 for visibility. The solid lines represent the cross section from pp data at the same rapidity interval scaled by the same 10^2 factor. Figure taken from [79]

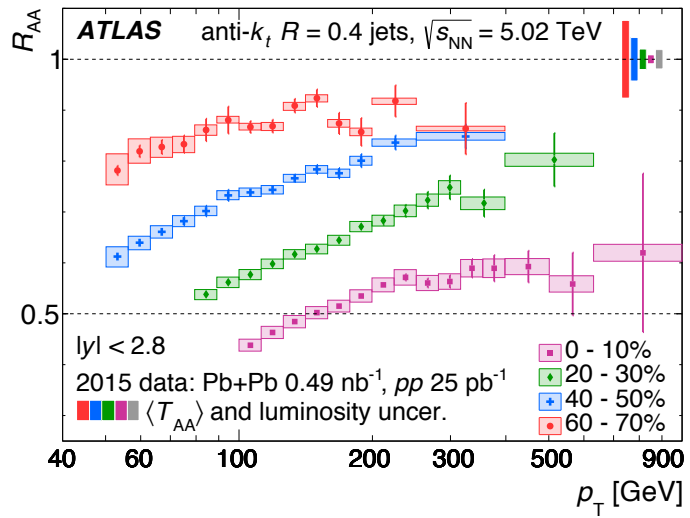


Figure 3.4: The R_{AA} distributions as a function of jet p_T for different centrality bins and jet rapidity $|y| < 2.8$. The error bars represent statistical uncertainties while the shaded boxes represent systematic uncertainties. Figure taken from [79]

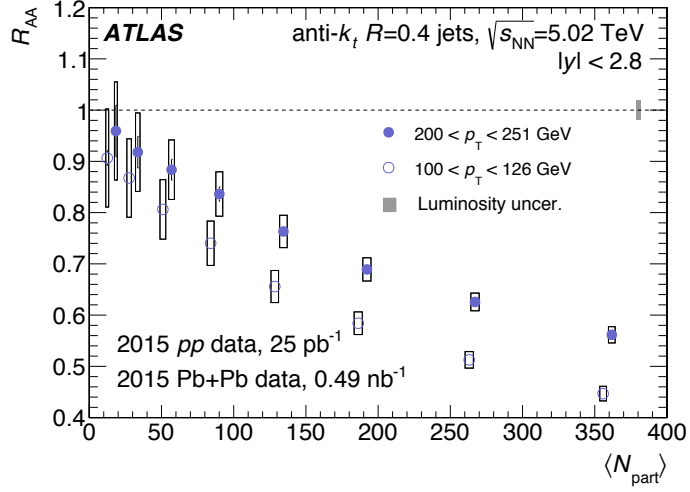


Figure 3.5: The R_{AA} distributions as a function of jet p_T for different centrality bins and jet rapidity $|y| < 2.8$. The error bars represent statistical uncertainties while the shaded boxes represent systematic uncertainties. Figure taken from [79]

316 3.3 Jet Fragmentation

Chapter 4

Experimental Setup

Chapter 5

ATLAS Qualification Task

Chapter 6

Measurement of Angular Correlations Between Tracks And Jets

Bibliography

- [1] G. Roland, K. Safarik and P. Steinberg, *Heavy-ion collisions at the LHC*, Prog. Part. Nucl. Phys. **77** (2014) 70 (cit. on p. 1).
- [2] W. Busza et al., *Heavy Ion Collisions: The Big Picture, and the Big Questions*, Ann. Rev. Nucl. Part. Sci. **68** (2018) 339, arXiv: [1802.04801 \[hep-ph\]](#) (cit. on pp. 1, 7).
- [3] M. K. Gaillard, P. D. Grannis and F. J. Sciulli, *The Standard model of particle physics*, Rev. Mod. Phys. **71** (1999) S96, arXiv: [hep-ph/9812285 \[hep-ph\]](#) (cit. on p. 3).
- [4] J Beringer et al., *Review of Particle Physics, 2012-2013. Review of Particle Properties*, Phys. Rev. D **86** (2012) 010001 (cit. on pp. 4, 5).
- [5] A. Deur et al., *High precision determination of the Q^2 evolution of the Bjorken Sum*, Phys. Rev. **D90** (2014) 012009, arXiv: [1405.7854 \[nucl-ex\]](#) (cit. on p. 6).
- [6] J. H. Kim et al., *A Measurement of $\alpha_s(Q^2)$ from the Gross-Llewellyn Smith sum rule*, Phys. Rev. Lett. **81** (1998) 3595, arXiv: [hep-ex/9808015 \[hep-ex\]](#) (cit. on p. 6).
- [7] G. Altarelli et al., *Determination of the Bjorken sum and strong coupling from polarized structure functions*, Nucl. Phys. **B496** (1997) 337, arXiv: [hep-ph/9701289 \[hep-ph\]](#) (cit. on p. 6).
- [8] H. W. Kendall, *Deep inelastic scattering: Experiments on the proton and the observation of scaling*, Rev. Mod. Phys. **63** (3 1991) 597 (cit. on p. 6).
- [9] A. L. Kataev, G. Parente and A. V. Sidorov, *Improved fits to the xF_3 CCFR data at the next-to-next-to-leading order and beyond*, Phys. Part. Nucl. **34** (2003) 20, [Erratum: Phys. Part. Nucl.38,no.6,827(2007)], arXiv: [hep-ph/0106221 \[hep-ph\]](#) (cit. on p. 6).
- [10] S. Alekhin, J. Blumlein and S. Moch, *Parton Distribution Functions and Benchmark Cross Sections at NNLO*, Phys. Rev. **D86** (2012) 054009, arXiv: [1202.2281 \[hep-ph\]](#) (cit. on p. 6).
- [11] S. Alekhin, J. Blumlein and S.-O. Moch, *ABM news and benchmarks*, PoS **DIS2013** (2013) 039, arXiv: [1308.5166 \[hep-ph\]](#) (cit. on p. 6).

- [340] [12] J. Blumlein, H. Bottcher and A. Guffanti, *Non-singlet QCD analysis of deep inelastic world data at $O(\alpha_s^3)$* , Nucl. Phys. **B774** (2007) 182, arXiv: [hep-ph/0607200 \[hep-ph\]](#) (cit. on p. 6).
- [341] [13] H1 Collaboration, *Three- and Four-jet Production at Low x at HERA*, Eur. Phys. J. **C54** (2008) 389, arXiv: [0711.2606 \[hep-ex\]](#) (cit. on p. 6).
- [342] [14] ZEUS Collaboration, *Forward-jet production in deep inelastic ep scattering at HERA*, Eur. Phys. J. **C52** (2007) 515, arXiv: [0707.3093 \[hep-ex\]](#) (cit. on p. 6).
- [343] [15] ZEUS Collaboration, *Multi-jet cross-sections in charged current $e^\pm p$ scattering at HERA*, Phys. Rev. **D78** (2008) 032004, arXiv: [0802.3955 \[hep-ex\]](#) (cit. on p. 6).
- [344] [16] ZEUS Collaboration, *Inclusive dijet cross sections in neutral current deep inelastic scattering at HERA*, Eur. Phys. J. **C70** (2010) 965, arXiv: [1010.6167 \[hep-ex\]](#) (cit. on p. 6).
- [345] [17] ZEUS Collaboration, *Inclusive-jet cross sections in NC DIS at HERA and a comparison of the kT , anti- kT and SIScone jet algorithms*, Phys. Lett. **B691** (2010) 127, arXiv: [1003.2923 \[hep-ex\]](#) (cit. on p. 6).
- [346] [18] H1 Collaboration, *Jet Production in ep Collisions at High Q^2 and Determination of α_s* , Eur. Phys. J. **C65** (2010) 363, arXiv: [0904.3870 \[hep-ex\]](#) (cit. on p. 6).
- [347] [19] E. V. Shuryak, *Quantum chromodynamics and the theory of superdense matter*, Physics Reports **61** (1980) 71, ISSN: 0370-1573 (cit. on pp. 6, 11).
- [348] [20] R. Glauber, *Lectures in theoretical physics*, ed. WE Brittin and LG Dunham, Interscience, New York **1** (1959) 315 (cit. on p. 7).
- [349] [21] R. Glauber et al., *Lectures in theoretical physics*, 1959 (cit. on p. 7).
- [350] [22] H. D. Vries, C. D. Jager and C. D. Vries, *Nuclear charge-density-distribution parameters from elastic electron scattering*, Atomic Data and Nuclear Data Tables **36** (1987) 495, ISSN: 0092-640X (cit. on pp. 7, 8).
- [351] [23] M. L. Miller, K. Reygers, S. J. Sanders and P. Steinberg, *Glauber Modeling in High-Energy Nuclear Collisions*, Annual Review of Nuclear and Particle Science **57** (2007) 205, eprint: <https://doi.org/10.1146/annurev.nucl.57.090506.123020> (cit. on pp. 7, 8, 10, 23).
- [352] [24] B. Alver, M. Baker, C. Loizides and P. Steinberg, *The PHOBOS Glauber Monte Carlo*, (2008), arXiv: [0805.4411 \[nucl-ex\]](#) (cit. on p. 7).
- [353] [25] D. Kharzeev and M. Nardi, *Hadron production in nuclear collisions at RHIC and high density QCD*, Phys. Lett. **B507** (2001) 121, arXiv: [nucl-th/0012025 \[nucl-th\]](#) (cit. on p. 9).

- 370 [26] A. Bialas, M. Bleszynski and W. Czyz, *Multiplicity Distributions in Nucleus-Nucleus Collisions at*
 371 *High-Energies*, Nucl. Phys. **B111** (1976) 461 (cit. on p. 9).
- 372 [27] ATLAS Collaboration, *Centrality determination in $\sqrt{s_{NN}} = 5.02 \text{ TeV Pb+Pb collision data in 2015}$* ,
 373 tech. rep. ATL-COM-PHYS-2016-1287, CERN, 2016 (cit. on p. 10).
- 374 [28] J. C. Collins and M. J. Perry, *Superdense Matter: Neutrons or Asymptotically Free Quarks?*, Phys. Rev.
 375 Lett. **34** (21 1975) 1353 (cit. on p. 11).
- 376 [29] A. D. Linde, *Phase transitions in gauge theories and cosmology*, Reports on Progress in Physics **42**
 377 (1979) 389 (cit. on p. 11).
- 378 [30] S. B. Ruster, V. Werth, M. Buballa, I. A. Shovkovy and D. H. Rischke, *Phase diagram of neutral quark*
 379 *matter: Self-consistent treatment of quark masses*, Phys. Rev. D **72** (3 2005) 034004 (cit. on p. 11).
- 380 [31] PHENIX Collaboration, *Enhanced Production of Direct Photons in Au + Au Collisions at $\sqrt{s_{NN}} =$*
 381 *200 GeV and Implications for the Initial Temperature*, Phys. Rev. Lett. **104** (13 2010) 132301 (cit. on
 382 p. 11).
- 383 [32] ALICE Collaboration, *Direct photon production in Pb-Pb collisions at $s_{NN}=2.76 \text{ TeV}$* , Physics Letters
 384 B **754** (2016) 235, ISSN: 0370-2693 (cit. on p. 11).
- 385 [33] Z. Fodor and S. Katz, *Critical point of QCD at finite T and λ , lattice results for physical quark masses*,
 386 Journal of High Energy Physics **2004** (2004) 050 (cit. on p. 11).
- 387 [34] STAR Collaboration, *Experimental and theoretical challenges in the search for the quark-gluon plasma:*
 388 *The STAR Collaboration's critical assessment of the evidence from RHIC collisions*, Nuclear Physics A
 389 **757** (2005) 102, First Three Years of Operation of RHIC, ISSN: 0375-9474 (cit. on p. 11).
- 390 [35] ALICE Collaboration, *Production of light nuclei and anti-nuclei in pp and Pb-Pb collisions at energies*
 391 *available at the CERN Large Hadron Collider*, Phys. Rev. C **93** (2 2016) 024917 (cit. on p. 11).
- 392 [36] PHENIX Collaboration, *Single identified hadron spectra from $\sqrt{s_{NN}} = 130 \text{ GeV Au + Au collisions}$* ,
 393 Phys. Rev. C **69** (2 2004) 024904 (cit. on p. 11).
- 394 [37] BRAHMS Collaboration, *Centrality dependent particle production at $y = 0$ and $y \geq 1$ in Au+Au collisions*
 395 *at $\sqrt{s_{NN}} = 200 \text{ GeV}$* , Phys. Rev. C **72** (1 2005) 014908 (cit. on p. 11).
- 396 [38] PHOBOS Collaboration, *Identified hadron transverse momentum spectra in Au+Au collisions at*
 397 *$\sqrt{s_{NN}} = 62.4 \text{ GeV}$* , Phys. Rev. C **75** (2 2007) 024910 (cit. on p. 11).
- 398 [39] ALICE Collaboration, *Centrality dependence of π , K , and p production in Pb-Pb collisions at $\sqrt{s_{NN}} =$*
 399 *2.76 TeV*, Phys. Rev. C **88** (4 2013) 044910 (cit. on p. 11).

- 400 [40] ATLAS Collaboration, *Measurement of the azimuthal anisotropy of charged particles produced in $\sqrt{s_{NN}} =$*
 401 *5.02 TeV Pb+Pb collisions with the ATLAS detector*, Eur. Phys. J. **C78** (2018) 997, arXiv: [1808.03951](#)
 402 [[nucl-ex](#)] (cit. on p. [12](#)).
- 403 [41] PHENIX Collaboration, *Elliptic Flow of Identified Hadrons in Au + Au Collisions at $\sqrt{s_{NN}} = 200$*
 404 *GeV*, Phys. Rev. Lett. **91** (18 2003) 182301 (cit. on p. [12](#)).
- 405 [42] CMS Collaboration, *Non-Gaussian elliptic-flow fluctuations in PbPb collisions at $\sqrt{s_{NN}} = 5.02$ TeV*,
 406 Phys. Lett. **B789** (2019) 643, arXiv: [1711.05594](#) [[nucl-ex](#)] (cit. on p. [12](#)).
- 407 [43] ALICE Collaboration, *Anisotropic Flow of Charged Particles in Pb-Pb Collisions at $\sqrt{s_{NN}} = 5.02$ TeV*,
 408 Phys. Rev. Lett. **116** (13 2016) 132302 (cit. on p. [12](#)).
- 409 [44] M. Connors, C. Nattrass, R. Reed and S. Salur, *Jet measurements in heavy ion physics*, Rev. Mod.
 410 Phys. **90** (2 2018) 025005 (cit. on p. [12](#)).
- 411 [45] A. M. Poskanzer and S. A. Voloshin, *Methods for analyzing anisotropic flow in relativistic nuclear*
 412 *collisions*, Phys. Rev. **C58** (1998) 1671, arXiv: [nucl-ex/9805001](#) [[nucl-ex](#)] (cit. on p. [12](#)).
- 413 [46] U. Heinz and R. Snellings, *Collective flow and viscosity in relativistic heavy-ion collisions*, Ann. Rev.
 414 Nucl. Part. Sci. **63** (2013) 123, arXiv: [1301.2826](#) [[nucl-th](#)] (cit. on p. [12](#)).
- 415 [47] H. Niemi, K. J. Eskola and R. Paatelainen, *Event-by-event fluctuations in a perturbative QCD +*
 416 *saturation + hydrodynamics model: Determining QCD matter shear viscosity in ultrarelativistic heavy-*
 417 *ion collisions*, Phys. Rev. **C93** (2016) 024907, arXiv: [1505.02677](#) [[hep-ph](#)] (cit. on p. [13](#)).
- 418 [48] ALICE Collaboration, *Higher harmonic anisotropic flow measurements of charged particles in Pb-Pb*
 419 *collisions at $\sqrt{s_{NN}} = 2.76$ TeV*, Phys. Rev. Lett. **107** (2011) 032301, arXiv: [1105.3865](#) [[nucl-ex](#)]
 420 (cit. on p. [13](#)).
- 421 [49] J. D. Bjorken, *Highly relativistic nucleus-nucleus collisions: The central rapidity region*, Phys. Rev. D
 422 **27** (1 1983) 140 (cit. on p. [12](#)).
- 423 [50] PHENIX Collaboration, *Formation of dense partonic matter in relativistic nucleus-nucleus collisions at*
 424 *RHIC: Experimental evaluation by the PHENIX collaboration*, Nucl. Phys. **A757** (2005) 184, arXiv:
 425 [nucl-ex/0410003](#) [[nucl-ex](#)] (cit. on p. [13](#)).
- 426 [51] CMS Collaboration, *Charged hadron multiplicity and transverse energy densities in PbPb collisions*
 427 *from CMS*, Journal of Physics G: Nuclear and Particle Physics **38** (2011) 124041 (cit. on p. [13](#)).
- 428 [52] B. Muller, J. Schukraft and B. Wyslouch, *First Results from Pb+Pb collisions at the LHC*, Ann. Rev.
 429 Nucl. Part. Sci. **62** (2012) 361, arXiv: [1202.3233](#) [[hep-ex](#)] (cit. on p. [14](#)).

- [53] T. Sjostrand, S. Mrenna and P. Z. Skands, *A Brief Introduction to PYTHIA 8.1*, Comput. Phys. Commun. **178** (2008) 852, arXiv: [0710.3820 \[hep-ph\]](#) (cit. on p. 13).
- [54] G.-Y. Qin and X.-N. Wang, *Jet quenching in high-energy heavy-ion collisions*, Int. J. Mod. Phys. E **24** (2015) 1530014, [,309(2016)], arXiv: [1511.00790 \[hep-ph\] \[hep-ph\]](#) (cit. on pp. 13, 14, 17).
- [55] A. D. Martin, W. J. Stirling, R. S. Thorne and G. Watt, *Parton distributions for the LHC*, The European Physical Journal C **63** (2009) 189, ISSN: 1434-6052, URL: <https://doi.org/10.1140/epjc/s10052-009-1072-5> (cit. on p. 15).
- [56] M. Hirai, S. Kumano and T.-H. Nagai, *Determination of nuclear parton distribution functions and their uncertainties at next-to-leading order*, Phys. Rev. C **76** (6 2007) 065207 (cit. on p. 16).
- [57] D. de Florian and R. Sassot, *Nuclear parton distributions at next to leading order*, Phys. Rev. D **69** (7 2004) 074028 (cit. on p. 16).
- [58] K. Eskola, H Paukkunen and C. Salgado, *EPS09 — A new generation of NLO and LO nuclear parton distribution functions*, Journal of High Energy Physics **2009** (2009) 065 (cit. on p. 16).
- [59] S. J. Brodsky and H. J. Lu, *Shadowing and antishadowing of nuclear structure functions*, Phys. Rev. Lett. **64** (12 1990) 1342 (cit. on p. 16).
- [60] European Muon Collaboration, *The ratio of the nucleon structure functions F2N for iron and deuterium*, Physics Letters B **123** (1983) 275, ISSN: 0370-2693 (cit. on p. 16).
- [61] O. Hen, E. Piasetzky and L. B. Weinstein, *New data strengthen the connection between short range correlations and the EMC effect*, Phys. Rev. C **85** (4 2012) 047301 (cit. on p. 16).
- [62] K. Saito and T. Uchiyama, *Effect of the Fermi Motion on Nuclear Structure Functions and the Emc Effect*, Z. Phys. **A322** (1985) 299 (cit. on p. 16).
- [63] CMS Collaboration, *Jet momentum dependence of jet quenching in PbPb collisions at sNN=2.76 TeV*, Physics Letters B **712** (2012) 176, ISSN: 0370-2693 (cit. on p. 16).
- [64] ATLAS collaboration, *Study of inclusive jet yields in Pb+Pb collisions at $\sqrt{s_{NN}} = 5.02$ TeV*, (2017) (cit. on p. 16).
- [65] The CMS collaboration, *Measurement of transverse momentum relative to dijet systems in PbPb and pp collisions at $\sqrt{s_{NN}} = 2.76$ TeV*, Journal of High Energy Physics **2016** (2016) 6, ISSN: 1029-8479, URL: [https://doi.org/10.1007/JHEP01\(2016\)006](https://doi.org/10.1007/JHEP01(2016)006) (cit. on p. 16).
- [66] S. Chatrchyan et al., *Jet momentum dependence of jet quenching in PbPb collisions at $\sqrt{s_{NN}} = 2.76$ TeV*, Phys. Lett. **B712** (2012) 176, arXiv: [1202.5022 \[nucl-ex\]](#) (cit. on p. 16).

- [67] R. Baier, Y. Dokshitzer, A. Mueller, S. Peigné and D. Schiff, *Radiative energy loss of high energy quarks and gluons in a finite-volume quark-gluon plasma*, Nuclear Physics B **483** (1997) 291, ISSN: 0550-3213 (cit. on p. 17).
- [68] M. Gyulassy, P. Levai and I. Vitev, *Jet quenching in thin quark gluon plasmas. 1. Formalism*, Nucl. Phys. **B571** (2000) 197, arXiv: [hep-ph/9907461 \[hep-ph\]](#) (cit. on p. 17).
- [69] U. A. Wiedemann, *Gluon radiation off hard quarks in a nuclear environment: Opacity expansion*, Nucl. Phys. **B588** (2000) 303, arXiv: [hep-ph/0005129 \[hep-ph\]](#) (cit. on p. 17).
- [70] P. B. Arnold, G. D. Moore and L. G. Yaffe, *Photon emission from ultrarelativistic plasmas*, JHEP **11** (2001) 057, arXiv: [hep-ph/0109064 \[hep-ph\]](#) (cit. on p. 17).
- [71] X.-F. Guo and X.-N. Wang, *Multiple scattering, parton energy loss and modified fragmentation functions in deeply inelastic e A scattering*, Phys. Rev. Lett. **85** (2000) 3591, arXiv: [hep-ph/0005044 \[hep-ph\]](#) (cit. on p. 17).
- [72] M. Cacciari, G. P. Salam and G. Soyez, *The Anti- $k(t)$ jet clustering algorithm*, JHEP **0804** (2008) 063, arXiv: [0802.1189 \[hep-ph\]](#) (cit. on pp. 17, 18).
- [73] S. Catani, Y. L. Dokshitzer, M. H. Seymour and B. R. Webber, *Longitudinally invariant K_t clustering algorithms for hadron hadron collisions*, Nucl. Phys. **B406** (1993) 187 (cit. on p. 18).
- [74] Y. L. Dokshitzer, G. D. Leder, S. Moretti and B. R. Webber, *Better jet clustering algorithms*, JHEP **08** (1997) 001, arXiv: [hep-ph/9707323 \[hep-ph\]](#) (cit. on p. 18).
- [75] G. P. Salam, *Towards Jetography*, Eur. Phys. J. **C67** (2010) 637, arXiv: [0906.1833 \[hep-ph\]](#) (cit. on pp. 18, 19).
- [76] G. P. Salam and G. Soyez, *A practical seedless infrared-safe cone jet algorithm*, Journal of High Energy Physics **2007** (2007) 086 (cit. on p. 19).
- [77] ATLAS Collaboration, *Measurement of the jet radius and transverse momentum dependence of inclusive jet suppression in lead-lead collisions at $\sqrt{s_{NN}} = 2.76$ TeV with the ATLAS detector*, Phys. Lett. **B719** (2013) 220, arXiv: [1208.1967 \[hep-ex\]](#) (cit. on p. 20).
- [78] ATLAS Collaboration, *Measurement of jet p_T correlations in Pb+Pb and pp collisions at $\sqrt{s_{NN}} = 2.76$ TeV with the ATLAS detector*, Phys. Lett. **B774** (2017) 379, arXiv: [1706.09363 \[hep-ex\]](#) (cit. on pp. 21–23).

- 488 [79] ATLAS Collaboration, *Measurement of the nuclear modification factor for inclusive jets in Pb+Pb*
489 *collisions at $\sqrt{s_{NN}} = 5.02 \text{ TeV}$ with the ATLAS detector*, *Phys. Lett.* **B790** (2019) 108, arXiv: 1805.
490 05635 [[nucl-ex](#)] (cit. on pp. 22, 24, 25).